Publisher: NPG; Journal: Nature: Nature; Article Type: Biology letter
DOI: 10.1038/nature13991

Native structure of photosystem II at 1.95 Å resolution viewed by femtosecond X-ray pulses

Michihiro Suga[1]*, Fusamichi Akita[1]*, Kunio Hirata[2,3], Go Ueno[2], Hironori Murakami[2], Yoshiki Nakajima[1], Tetsuya Shimizu[1], Keitaro Yamashita[2], Masaki Yamamoto[2], Hideo Ago[2] & Jian-Ren Shen[1]

[1]Photosynthesis Research Center, Graduate School of Natural Science and Technology, Okayama University, 3-1-1 Tsushima Naka, Okayama 700-8530, Japan.

[2]RIKEN SPring-8 Center, 1-1-1 Kouto Sayo, Hyogo 679-5148, Japan.

[3]Japan Science and Technology Agency (JST), Core Research for Evolutional Science and Technology (CREST), Kawaguchi, Saitama 332-0012, Japan.

*These authors contributed equally to this work.

Photosynthesis converts light energy into biologically useful chemical energy vital to life on Earth. The initial reaction of photosynthesis takes place in photosystem II (PSII), a 700-kilodalton homodimeric membrane protein complex which catalyses photo-oxidation of water into dioxygen through an S-state cycle of the oxygen evolving complex (OEC). The structure of PSII has been solved by X-ray diffraction (XRD) at 1.9-ångström (Å) resolution, which revealed that the OEC is a Mn_4CaO_5-cluster coordinated by a well-defined protein environment[1]. However, extended X-ray absorption fine structure (EXAFS) studies showed that the manganese cations in the OEC are easily reduced by X-ray irradiation[2], and slight differences were found in the Mn–Mn distances between the results of XRD[1], EXAFS[3–7] and theoretical studies[8–14]. Here we report a 'radiation-damage-free' structure of PSII from *Thermosynechococcus vulcanus* in the S_1 state at a resolution of 1.95 Å using femtosecond X-ray pulses of the SPring-8 ångström compact free-electron laser (SACLA) and a huge number of large, highly isomorphous PSII crystals. Compared with the structure from XRD, the OEC in the X-ray free electron

laser structure has Mn–Mn distances that are shorter by 0.1–0.2 Å. The valences of each manganese atom were tentatively assigned as Mn1D(III), Mn2C(IV), Mn3B(IV) and Mn4A(III), based on the average Mn–ligand distances and analysis of the Jahn–Teller axis on Mn(III). One of the oxo-bridged oxygens, O5, has significantly longer Mn–O distances in contrast to the other oxo-oxygen atoms, suggesting that it is a hydroxide ion instead of a normal oxygen dianion and therefore may serve as one of the substrate oxygen atoms. These findings provide a structural basis for the mechanism of oxygen evolution, and we expect that this structure will provide a blueprint for design of artificial catalysts for water oxidation.

PSII is a multi-subunit pigment-protein complex embedded in the thylakoid membranes of higher plants, green algae and cyanobacteria, and is the only molecular machine capable of oxidizing water by use of visible light. Water molecules are split into electrons, hydrogen atoms and oxygen molecules at the catalytic centre of PSII, namely, the OEC, through four electron and/or proton removing steps as described in the S_i-state cycle (with i = 0–4, where i indicates the number of oxidative equivalents accumulated). Because of its ability to split water, the OEC is considered a promising template for the synthesis of artificial catalysts for water-splitting aimed at obtaining clean and renewable energy from sunlight, which is considered a promising way to supplement the consumption of limited and environmentally unfriendly fossil fuels.

In order to elucidate the mechanism of the water-splitting reaction, the structure of PSII has been studied extensively by XRD, with a resolution that has gradually increased from 3.8 to 1.9 Å using synchrotron radiation (SR) X-ray sources[1,15–18]. In particular, the SR structure of PSII at atomic resolution revealed that the OEC is a Mn_4CaO_5 cluster organized into a distorted-chair shape, in which the cuboidal part is composed of Mn_3CaO_3 and the outer manganese is attached via two μ-oxo-bridges[1]. The high-resolution structure also revealed that four water molecules are coordinated to the Mn_4CaO_5 cluster, among which, two are coordinated

to the Ca^{2+} ion and two are attached to the outer manganese[1] (designated Mn4A; the naming of the Mn ions employed in this study combines the nomenclatures of those used in the EXAFS[4] and XRD studies[1]). Although these provided an important structural basis for the mechanism of water-splitting, the average Mn–ligand and Mn–Mn distances were found to be slightly longer than those deduced from EXAFS[3–7] and from computational analysis based on the SR structure[8–14]. This has been suggested to result from radiation damage, as hydrated electrons generated by X-ray irradiation[19] are able to reduce metal catalytic centres (such as the OEC in PSII) rapidly, although the SR PSII structure at 1.9 Å resolution was obtained with an X-ray dose much reduced compared to those used previously[15–18]. Based on the EXAFS analysis, the dose used for collecting the SR structure at 1.9 Å resolution may cause 25% of the Mn ions in the OEC to be reduced to 2+ ions[2]. Such radiation damage to biological samples is inevitable with SR X-ray sources, since the shortest time to collect a diffraction image is of the order of one second, which is long enough for structural changes to occur upon breakage of covalent bonds by the radicals generated by the strong X-ray irradiation.

In order to eliminate the radiation damage, a new approach employing a femtosecond X-ray free electron laser (XFEL) has been developed which demonstrated that a radiation-damage-free structure may be obtained by using the ultra-short and high-brilliance XFEL pulses to collect diffraction images before the onset of radiation damage (a 'diffraction before destruction' approach)[20]. So far XFEL has been mainly used to collect diffraction data from nanocrystals using the method of serial femtosecond crystallography (SFX), in which a stream of nanometre-to-micrometre sized crystals flows across the XFEL beam and a large number of single-crystal diffraction data are collected in random orientations at room temperature, and the data obtained are processed by a Monte Carlo approach[21–23]. However, as diffraction intensities are proportional to the diffraction volume and inversely proportional to the unit cell volume[24], the resolution obtainable with this method is limited, especially for large

membrane protein complexes such as PSII and cytochrome *c* oxidase (C*c*O), whose unit cell volumes exceed 8 MÅ^3. In addition, the nanometre–micrometre sized crystals used for SFX are often obtained under sub-optimal conditions, and their properties are easily affected by post-crystallization handling procedures; all of these will limit the resolution of large membrane protein crystals. Very recently, it was demonstrated that a radiation-damage-free structure can be obtained from large crystals using the XFEL beam by collecting still diffraction images at a cryogenic temperature from well separated positions in a crystal and by using a number of large, highly isomorphous crystals. This method has been used successfully to obtain a radiation-damage-free structure of C*c*O at 1.9 Å resolution[25]. Here we determined the radiation-damage-free structure of PSII in the dark-stable S_1 state by use of this method and a huge number of large PSII crystals with high isomorphism.

Still diffraction images were collected with XFEL provided by SACLA and large PSII crystals (1.2 × 0.5 × 0.2 mm). Each irradiation point on a crystal was separated by 50 μm (Extended Data Fig. 1a, b), which has been shown to be enough to avoid the effect of radiation damage from the previous irradiation point[25] (see Methods). The crystals were rotated in steps of 0.2° following the previous irradiation, which was smaller than one-third of the typical mosaic spread of the PSII crystals; this ensured data quality high enough for the subsequent structural refinement[25]. Diffraction spots up to 1.85 Å resolution were observed (Extended Data Fig. 2); we collected two independent data sets, data set 1 with 5,592 still images from 254 crystals, and data set 2 with 2,058 images from 82 crystals, from which two complete data sets were processed, both to 1.95 Å resolution. The total absorbed dose and photon density of each irradiation point for both data sets were 1.4 MGy and 0.26×10^{10} photons per μm^2, respectively, which were approximately equal to that each irradiation point received in the SR data set used for the analysis of the 1.9 Å structure[1]. Structure analysis was performed as described in Methods, and the statistics for the diffraction experiments and structural refinement are given in

Extended Data Table 1. The R_{free} values were 0.238 (data set 1) and 0.225 (data set 2), which, together with the 1.95 Å resolution, allowed us to build the structure of the OEC unambiguously. In this structure, the positions of heavy metals were confirmed clearly, even in the anomalous difference Fourier map (Fig. 1a, Extended Data Fig. 3a, b). In fact, the *B*-factors for the OEC atoms (23.6 $Å^2$) were found to be lower than those observed in the overall protein atoms of both XFEL (35.1 $Å^2$) and SR (35.2 $Å^2$) structures (Table 1, Extended Data Tables 1 and 2), showing the reliability of the OEC structure. Nevertheless, we repeated the same experiments using the crystals from different preparations in the two data sets to verify the reproducibility of the bond distances within the OEC, which showed a very good agreement among the four PSII monomers in the two independent dimer structures.

The overall architecture of the OEC in the XFEL structure is very similar to that of the SR structure (PDB ID 3ARC), but distinct differences were observed in Mn–Mn and Mn–O distances (Figs 1b–d and 2a, Extended Data Table 3). For comparison, we take the average distances from four monomers of the two independent dimers, and the average Mn–Mn distances were 2.7 Å for Mn1D–Mn2C, 3.2 Å for Mn1D–Mn3B, 5.0 Å for Mn1D–Mn4A, 2.7 Å for Mn2C–Mn3B, 5.2 Å for Mn2C–Mn4A and 2.9 Å for Mn3B–Mn4A (Fig. 1b, Table 1, Extended Data Table 2). All of these distances were 0.1–0.2 Å shorter than those in the SR structure, in good accordance with the results of EXAFS[3–7] and theoretical calculations[8–14]. This clearly indicated that the X-ray damage possibly included in the previous SR structure has been eliminated. In particular, we assigned two 2.7 Å Mn–Mn vectors to Mn1D–Mn2C and Mn2C–Mn3B and one 2.8-2.9 Å vector to Mn3B–Mn4A; the presence of these three vectors has been suggested by precision EXAFS measurements, although their exact geometry may not be the same as that revealed from the crystal structure[3–7]. In contrast to the slightly shorter Mn–Mn distances, no clear differences were observed in the Mn–Ca distances compared with those in the SR structure (there were three proximal Mn–Ca distances with 3.5 Å for Mn1D–Ca, 3.3 Å for

Mn2C–Ca, 3.4 Å for Mn3B–Ca, and one distal distance of 3.8 Å for Mn4–Ca, see Fig. 1c, Table 1, Extended Data Table 3). The OEC model proposed from the EXAFS studies has possibly one to two interactions of Mn–Ca distance around 3.9 Å, which is different from the present XFEL structure[4].

A distinct feature of the SR OEC structure is the unusual position of O5, which binds weakly to Mn1D, Mn3B, Mn4A and Ca with distances ranging from 2.4 to 2.7 Å[1]. In the XFEL structure, the average bond distances were 2.2 Å for Mn3B–O5, 2.3 Å for Mn4A–O5, 2.7 Å for Mn1D–O5, and 2.5 Å for Ca–O5 (Fig. 1d, Table 1, Extended Data Table 3). Compared with the SR structure, three bond distances from O5 to Mn3B, Mn4A and Ca were shortened by 0.2 Å; in contrast, the distance to Mn1D was elongated by 0.1 Å. The longer Mn4A–O5 distance in the SR structure may imply that Mn4A has received some reduction by the attack of hydrated electrons generated by the radiation damage, leading to a longer distance to O5 in the SR structure; this in turn implies that Mn4A is more prone to radiation damage than Mn1D because of its dangling position which leads to a larger exposure to the solvent, whereas Mn1D exists in the solid cuboidal part of the structure with less exposure to the solvent. Recent computational studies failed to reproduce the long bond distances from O5 to the Mn ions, and instead resulted in strong binding to either Mn1D or Mn4A (with bond lengths shorter than 1.9 Å), giving rise to either R-type (right-side open) or L-type (left-side open) structures, when O5 is assumed to be in a deprotonated state[11,13]. Our XFEL structure showed that O5 indeed exists in a position closer to Mn4A than to Mn1D, however, such preference for Mn4A was much less than that shown by typical theoretical analyses, and the unusual nature of the bonds involving O5 is largely preserved. Therefore, we confirmed that the longer distances of μ-oxo bridges from O5 were an intrinsic and remarkable feature of the OEC structure, not an artefact of X-ray reduction. Based on this, we propose that O5 is a hydroxide ion rather than an oxygen dianion (deprotonated oxygen) in the S_1 state. Indeed, theoretical calculations based on the assumption that O5 is a

hydroxide ion have yielded long bond distances between O5 and nearby Mn ions that are largely comparable with the present XFEL structure[11,26].

Another feature of the Mn–O bond distances in the XFEL structure was that all of the oxo-bridges connected with Mn2C were 0.1–0.3 Å shorter than the corresponding distances in the previous SR structure[1], which may indicate that Mn2C was also partially photo-reduced in the SR structure. Furthermore, structural differences were also found in the ligand environment around the OEC between the XFEL and SR structures. All of the ligand groups coordinated to the OEC had slightly shorter distances, some of them faced in slightly different directions and some water molecules existed in different positions (Table 1, Fig. 2b and 2c, Extended Data Table 3). In contrast, no apparent differences were observed in the acceptor side (the bound plastoquinone acceptors Q_A and Q_B, and the non-haem iron) or the region surrounding Y_D (D2-Y160) in the D2 subunit.

Based on the current XFEL structure, all of the four Mn ions are six-coordinated (Extended Data Fig. 4a–d). The averaged ligand distances, including those to amino acids, oxo-bridges and terminal water ligands, are 2.1 Å for Mn1D, 2.0 Å for Mn2C, 2.0 Å for Mn3B and 2.1 Å for Mn4A (Extended Data Table 4). Because of the longer pair of Mn1D–O5/OD2 (D1-Asp342) and Mn4A–O5/W1 (one of the two water ligands to Mn4A) distances, the average ligand distances of Mn1D and Mn4A are slightly longer than those of Mn2C and Mn3B. These longer pairs also contributed to the non-uniform distribution of the ligand distances, which is a typical characteristic of Mn ions in the 3+ oxidation state having a Jahn–Teller axis (Extended Data Fig. 5a, b, Extended Data Table 4). Based on the high oxidation scenario—that the oxidation states of the four Mn ions are (III, III, IV, IV) in the S_1 state—we propose that the valences of Mn1D, Mn2C, Mn3B and Mn4A can be assigned as III, IV, IV and III, respectively. This assignment is supported by the near-centre localization of the O5 atom, as the III valence of the two Mn ions (Mn1D and Mn4A) connected to the two sides of the O5 atom would lead to a

longer and almost equal distance for the two Mn–O bonds as observed in the XFEL structure (Fig. 3). The assignment of Mn1D as in a 3+ valence state is consistent with the proposal from the combined study of multi-frequency electron paramagnetic resonance, ^{55}Mn-electron nuclear double-resonance and theoretical calculations showing that Mn1D is a 3+ ion in the S_2 state[27].

The present XFEL structure provides important clues to the mechanism of water oxidation. The unusual properties of O5 and the proposal that it is an OH^- ion in the S_1 state suggests that it is a water molecule in the S_0 state; upon transition from S_0 to S_1, a proton is released from the O5 site, leading to the OH^- species in the S_1 state. These inferences strongly suggest that O5 provides one of the substrate water molecules for the O=O bond formation, which is in agreement with recent ^{17}O electron-electron-double resonance-detected NMR experiments[28]. Based on the involvement of O5, formation of the O=O bond in the water oxidation reaction can proceed between O5 and another nearby oxygen atom, which could be a newly inserted water molecule, as proposed in ref. 29 and supported by a recent advanced EPR study[30] (Fig. 3). It should be pointed out, however, that the second oxygen atom might instead be provided by one of the already present terminal water ligands, W2 or W3, without imposing the insertion of a new water molecule (Fig. 3), as both W2 and W3 are within hydrogen-bond distances to O5 and therefore may be able to move towards to O5 to form the O–O bond during the S-state transition. Determination of which mechanism is correct will require further XFEL experiments to analyse the intermediate structures at atomic resolution, using the approach established in this study.

Received 30 August; accepted 21 October 2014; doi:10.1038/nature13991.

Published online XX 2014

1. Umena, Y., Kawakami, K., Shen, J. R. & Kamiya, N. Crystal structure of oxygen-evolving photosystem II at a resolution of 1.9 Å. *Nature* **473,** 55–60 (2011).

2. Yano, J. *et al.* X-ray damage to the Mn_4Ca complex in single crystals of photosystem II: a case study for metalloprotein crystallography. *Proc. Natl Acad. Sci. USA* **102,** 12047–12052 (2005).

3. Yano, J. *et al.* High-resolution Mn EXAFS of the oxygen-evolving complex in photosystem II: structural implications for the Mn_4Ca cluster. *J. Am. Chem. Soc.* **127,** 14974–14975 (2005).

4. Yano, J. *et al.* Where water is oxidized to dioxygen: structure of the photosynthetic Mn_4Ca cluster. *Science* **314,** 821–825 (2006).

5. Dau, H. & Haumann, M. The manganese complex of photosystem II in its reaction cycle — basic framework and possible realization at the atomic level. *Coord. Chem. Rev.* **252,** 273–295 (2008).

6. Dau, H., Grundmeier, A., Loja, P. & Haumann, M. On the structure of the manganese complex of photosystem II: extended-range EXAFS data and specific atomic-resolution models for four S-states. *Phil. Trans. R. Soc. Lond. B* **363,** 1237–1243 (2008).

7. Glöckner, C. *et al.* Structural changes of the oxygen-evolving complex in photosystem II during the catalytic cycle. *J. Biol. Chem.* **288,** 22607–22620 (2013). 8. Ames, W. *et al.* Theoretical evaluation of structural models of the S_2 state in the oxygen evolving complex of Photosystem II: protonation states and magnetic interactions. *J. Am. Chem. Soc.* **133,** 19743–19757 (2011).

9. Galstyan, A., Robertazzi, A. & Knapp, E. W. Oxygen-evolving Mn cluster in photosystem II: the protonation pattern and oxidation state in the high-resolution crystal structure. *J. Am. Chem. Soc.* **134,** 7442–7449 (2012).

10. Grundmeier, A. & Dau, H. Structural models of the manganese complex of photosystem II and mechanistic implications. *Biochim. Biophys. Acta* **1817,** 88–105 (2012).

11. Isobe, H. *et al.* Theoretical illumination of water-inserted structures of the $CaMn_4O_5$ cluster in the S_2 and S_3 states of oxygen-evolving complex of photosystem II: full geometry optimizations by B3LYP hybrid density functional. *Dalton Trans.* **41,** 13727–13740 (2012).

12. Luber, S. *et al.* S_1-state model of the O_2-evolving complex of photosystem II. *Biochemistry* **50,** 6308–6311 (2011).

13. Pantazis, D. A., Ames, W., Cox, N., Lubitz, W. & Neese, F. Two interconvertible structures that explain the spectroscopic properties of the oxygen-evolving complex of photosystem II in the S_2 state. *Angew. Chem. Int. Edn Engl.* **51,** 9935–9940 (2012).

14. Blomberg, M. R. A., Borowski, T., Himo, F., Liao, R. Z. & Siegbahn, P. E. M. Quantum chemical studies of mechanisms for metalloenzymes. *Chem. Rev.* **114,** 3601–3658 (2014).

15. Zouni, A. *et al.* Crystal structure of photosystem II from *Synechococcus elongatus* at 3.8 Å resolution. *Nature* **409,** 739–743 (2001).

16. Kamiya, N. & Shen, J. R. Crystal structure of oxygen-evolving photosystem II from *Thermosynechococcus vulcanus* at 3.7-Å resolution. *Proc. Natl Acad. Sci. USA* **100,** 98–103 (2003).

17. Ferreira, K. N., Iverson, T. M., Maghlaoui, K., Barber, J. & Iwata, S. Architecture of the photosynthetic oxygen-evolving center. *Science* **303,** 1831–1838 (2004).

18. Guskov, A. *et al.* Cyanobacterial photosystem II at 2.9-Å resolution and the role of quinones, lipids, channels and chloride. *Nature Struct. Mol. Biol.* **16,** 334–342 (2009).

19. Southworth-Davies, R. J., Medina, M. A., Carmichael, I. & Garman, E. F. Observation of decreased radiation damage at higher dose rates in room temperature protein crystallography. *Structure* **15,** 1531–1541 (2007).

20. Neutze, R., Wouts, R., van der Spoel, D., Weckert, E. & Hajdu, J. Potential for biomolecular imaging with femtosecond X-ray pulses. *Nature* **406,** 752–757 (2000).

21. Kern, J. *et al.* Simultaneous femtosecond X-ray spectroscopy and diffraction of photosystem II at room temperature. *Science* **340,** 491–495 (2013).

22. Kupitz, C. *et al.* Serial time-resolved crystallography of photosystem II using a femtosecond X-ray laser. *Nature* **513,** 261–265 (2014).

23. Kern, J. *et al.* Taking snapshots of photosynthetic water oxidation using femtosecond X-ray diffraction and spectroscopy. *Nature Commun.* **5,** 4371 (2014).

24. Holton, J. M. & Frankel, K. A. The minimum crystal size needed for a complete diffraction data set. *Acta Crystallogr. D* **66,** 393–408 (2010).

25. Hirata, K. *et al.* Determination of damage-free crystal structure of an X-ray-sensitive protein using an XFEL. *Nature Methods* **11,** 734–736 (2014).

26. Shoji, M. *et al.* Theoretical modeling of biomolecular systems I. Large scale QM/MM calculations of hydrogen bonding networks of oxygen evolving complex of photosystem II. *Mol. Phys.* http://dx.doi.org/10.1080/00268976.2014.960021 (published online 29 September 2014).

27. Cox, N. *et al.* Effect of Ca^{2+}/Sr^{2+} substitution on the electronic structure of the oxygen-evolving complex of photosystem II: a combined multifrequency EPR, ^{55}Mn-ENDOR, and DFT study of the S_2 state. *J. Am. Chem. Soc.* **133,** 3635–3648 (2011).

28. Rapatskiy, L. *et al.* Detection of the water-binding sites of the oxygen-evolving complex of Photosystem II using W-band ^{17}O electron-electron double resonance-detected NMR spectroscopy. *J. Am. Chem. Soc.* **134,** 16619–16634 (2012).

29. Siegbahn, P. E. Water oxidation mechanism in photosystem II, including oxidations, proton release pathways, O-O bond formation and O_2 release. *Biochim. Biophys. Acta* **1827,** 1003–1019 (2013).

30. Cox, N. *et al.* Electronic structure of the oxygen-evolving complex in photosystem II prior to O-O bond formation. *Science* **345,** 804–808 (2014).

Acknowledgements We thank T. Ishikawa, M. Yabashi, K. Tono and Y. Inubushi for help in using the SACLA beamline, T. Tsukihara and S. Yoshikawa for suggestions and comments on the experiments, F. Seno for assistance with sample preparation, and K. Kawakami and Y. Umena for suggestions in the initial stage of the project. F. H. M. Koua participated in the initial stage of this work. This work was supported by an X-ray Free Electron Laser Priority Strategy Program (The Ministry of Education, Culture, Sports, Science and Technology of Japan, MEXT) (H.A. and J.-R.S.), a JST/CREST grant (K.H.), a grant-in-aid for Specially Promoted Research no. 24000018 (J.-R.S.) and KAKENHI grant no. 26840023 (M.S.) from JSPS, MEXT, Japan. The XFEL experiments were performed at beamline 3 of SACLA with the approval of the Japan Synchrotron Radiation Research Institute (JASRI) (proposal nos 2012A8011, 2012B8040, 2013A8047, 2013B8052 and 2014A8036), and we thank staff at SACLA for their help.

Author Contributions H.A. and J.-R.S. planned and organized the experiments, F.A. and Y.N. prepared the samples, F.A. made the crystals, G.U., H.M., K.H., H.A. and M.Y. designed and established the experimental set-up, M.S., F.A., T.S., Y.N., G.U., H.M., K.H., H.A., M.Y. and J.-R.S. conducted the diffraction experiments, K.Y. performed scaling of raw diffraction images, M.S. performed the structural analysis, M.S. and J.-R.S. wrote the manuscript, and all authors discussed and commented on the results and the manuscript.

Author Information Coordinates and structure factors for the structure determination have been deposited in the Protein Data Bank with accession codes 4UB6 and 4UB8 for datasets 1 and 2, respectively. Reprints and

permissions information is available at www.nature.com/reprints. The authors declare no competing financial interests. Readers are welcome to comment on the online version of the paper. Correspondence and requests for materials should be addressed to H.A. (ago@spring8.or.jp), M.Y. (yamamoto@riken.jp) or J.-R.S. (shen@cc.okayama-u.ac.jp).

Figure 1 | Atomic structure of the OEC by XFEL. a, Electron density maps of the OEC. Grey, $2mF_o - DF_c$ map contoured at 7σ; **[AUTHOR: is sigma OK here and elsewhere? Text was corrupted]** magenta, $2mF_o - DF_c$ map contoured at 15σ; green, $mF_o - DF_c$ map contoured at 6σ. The $2mF_o - DF_c$ map was calculated before placing any atoms in the OEC, and the $mF_o - DF_c$ map was calculated after introducing the manganese and calcium atoms but without the oxygen atoms and water molecules. Colour codes for atoms: grey, manganese; blue, calcium; red, oxo-oxygen; yellow, O5; orange, water. Numbers 1–4 in the red spheres indicate O1–O4 atoms, and 1D, 2C, 3B and 4A indicate the four manganese ions named by a combination of crystal structure and previous EXAFS numbering. **b**, Mn–Mn distances in the OEC (in Å). Roman numerals in the spheres indicate the valence of manganese atoms assigned in this work. Oxygen atoms in the OEC are shown pink. **c**, Mn–Ca distances in the OEC (in Å). **d**, Mn–O, Ca–O, Mn–water and Ca–water distances in the OEC (in Å).

Figure 2 | Comparison of the OEC structures obtained by XFEL and SR. a, Superposition of three OEC structures, two from XFEL and one from SR. The OEC is depicted as in Fig. 1a. **b**, Superposition of the OEC and its ligand environment from the three structures. For clarity, the structures are rotated relative to that shown in **a**. Additional water molecules close to the OEC are also shown as spheres. **c**, An enlarged view of the region boxed by red dashed lines in **b**. In all three panels, the structure from XFEL data set 1 is coloured by atomic element as in Fig. 1a. Structures from XFEL data set 2 and SR are coloured in green and purple, respectively.

Figure 3 | Possible mechanisms for the oxygen-evolving reaction. O5 in the S_1 state is connected to both Mn1D(III) and Mn4A(III). Upon transition from S_1 to S_2, an electron may be removed from Mn4A, leading to a right-side open structure ('R-type'), or from Mn1D, leading to a left-side open structure ('L-type'). Both structures will allow insertion of a new water molecule during the subsequent S-state transition, preparing for the transit state immediately before O=O bond (indicated by a red bond in the right side of the bottom row) formation. Alternatively, the transit state ready for O=O bond formation may be formed by moving either W2 or W3 towards O5 (indicated by orange arrows in the left side of the bottom row). See text for more details. Colour code is the same as Fig. 1a.

Publisher: NPG; Journal: Nature: Nature; Article Type: Biology letter
DOI: 10.1038/nature13991

Table 1 | OEC interatomic distances obtained using XFEL and SR techniques

	XFEL	SR		XFEL	SR		XFEL
Mn–Mn			**Ca–O**			**B-factor**	
Mn1D–Mn2C	2.68 (0.05)*	2.8	Ca–O1	2.61 (0.03)*	2.4	Mn1D	23.4 (3.3)*
Mn1D–Mn3B	3.20 (0.08)*	3.3	Ca–O2	2.67 (0.06)*	2.5	Mn2C	23.4 (1.4)*
Mn1D–Mn4A	4.95 (0.04)*	5.0	Ca–O5	2.54 (0.08)*	2.7	Mn3B	22.0 (2.2)*
Mn2C–Mn3B	2.70 (0.03)*	2.9				Mn4A	23.4 (1.6)*
Mn2C–Mn4A	5.21 (0.04)*	5.4	**Water**			Ca	33.0 (3.8)*
Mn3B–Mn4A	2.87 (0.03)*	3.0	Mn4A–W1	2.25 (0.08)*	2.2	O1	23.3 (3.6)*
			Mn4A–W2	2.10 (0.09)*	2.2	O2	22.6 (2.1)*
Mn–Ca			Ca–W3	2.60 (0.01)*	2.4	O3	26.3 (6.5)*
Mn1D–Ca	3.47 (0.03)*	3.5	Ca–W4	2.47 (0.04)*	2.5	O4	20.7 (2.1)*
Mn2C–Ca	3.32 (0.03)*	3.4	O5–W2	3.00 (0.09)*	3.1	O5	17.7 (2.3)*
						Overall	
Mn3B–Ca	3.40 (0.06)*	3.4	O5–W3	3.12 (0.13)*	3.1	OEC	23.6 (2.0)*
Mn4A–Ca	3.77 (0.06)*	3.8	W2–W3	3.26 (0.09)*	3.3	All atoms	35.1
Mn–O			**Ligand**				
Mn1D–O1	1.80 (0.05)*	1.9	Mn1D–E189	1.79 (0.02)*	1.9		
Mn1D–O3	1.87 (0.08)*	1.8	Mn1D–H332	2.12 (0.03)*	2.2		
Mn1D–O5	2.70 (0.01)*	2.6	Mn1D–D342	2.22 (0.05)*	2.3		
Mn2C–O1	1.82 (0.07)*	2.1	Mn2C–D342	2.13 (0.04)*	2.2		
Mn2C–O2	1.83 (0.07)*	2.1	Mn2C–A344	1.90 (0.06)*	2.0		
Mn2C–O3	2.02 (0.06)*	2.1	Mn2C–E354†	2.13 (0.05)*	2.2		
Mn3B–O2	1.90 (0.12)*	1.9	Mn3B–E333	2.06 (0.03)*	2.1		
Mn3B–O3	2.06 (0.07)*	2.1	Mn3B–E354†	2.13 (0.02)*	2.2		
Mn3B–O4	1.90 (0.02)*	2.1	Mn4A–D170	2.03 (0.04)*	2.1		
Mn3B–O5	2.20 (0.14)*	2.4	Mn4A–E333	2.08 (0.02)*	2.2		
Mn4A–O4	2.02 (0.05)*	2.1	Ca–D170	2.36 (0.08)*	2.4		
Mn4A–O5	2.33 (0.03)*	2.5	Ca–A344	2.43 (0.01)*	2.5		

The Mn–Mn, Mn–Ca, Mn–O, Ca–O, water and ligand distances are given in Å. Values for the XFEL structure are the average of four monomers, whereas values for the SR structure are the average of two monomers.

*Numbers in parentheses represent standard derivations calculated from four PSII monomers. For the individual values in each monomer, see Extended Data Table 2.

†Residue from the CP43 protein.

Publisher: NPG; Journal: Nature: Nature; Article Type: Biology letter
DOI: 10.1038/nature13991

Publisher: NPG; Journal: Nature: Nature; Article Type: Biology letter
DOI: 10.1038/nature13991

Fig. 1

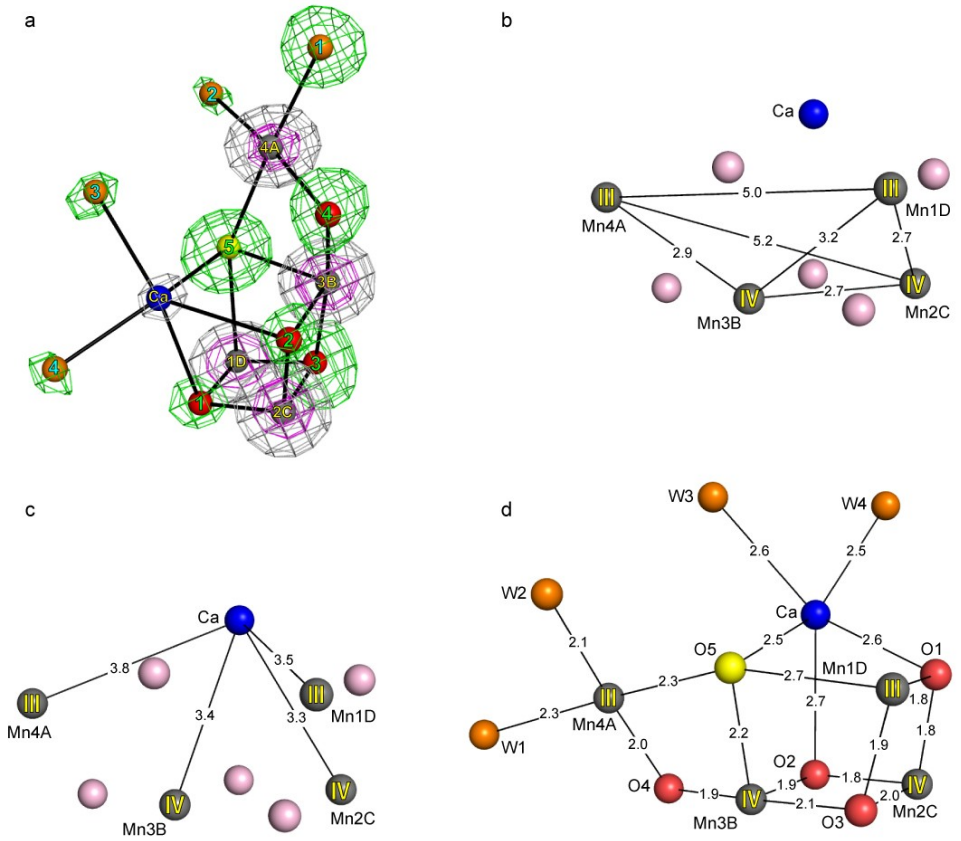

Publisher: NPG; Journal: Nature: Nature; Article Type: Biology letter
DOI: 10.1038/nature13991

Fig. 2

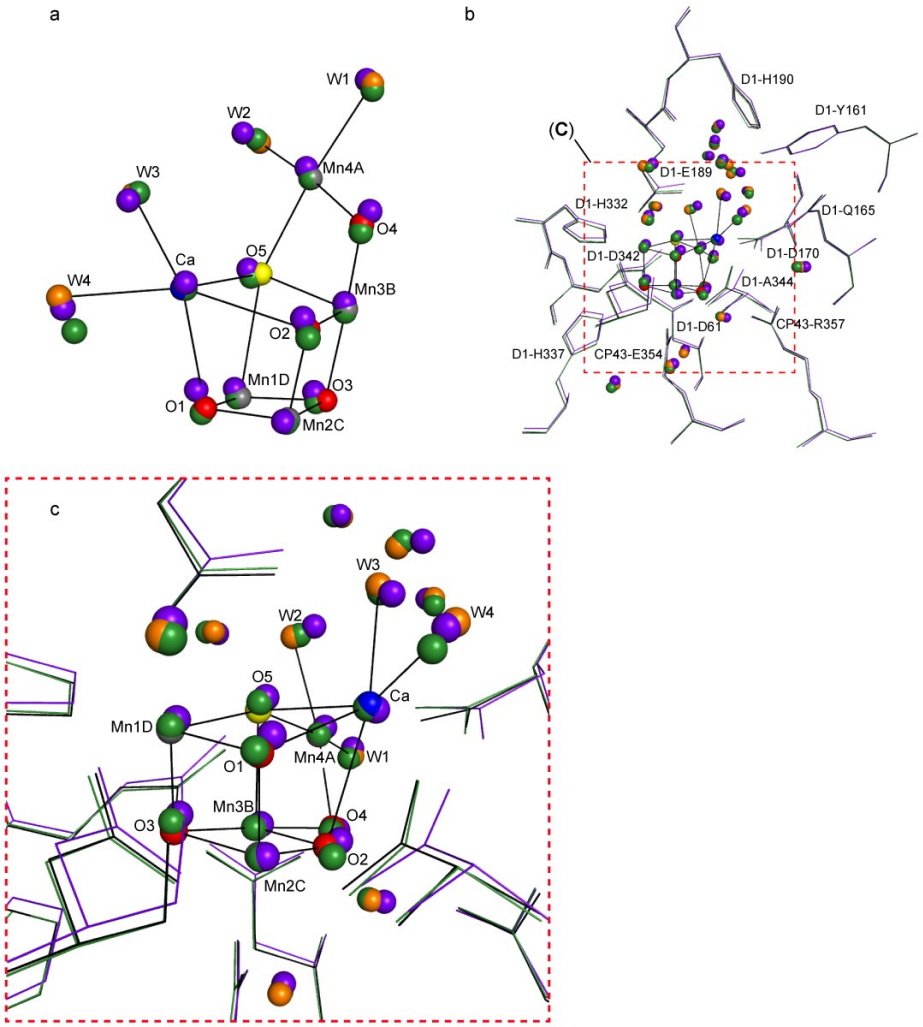

Publisher: NPG; Journal: Nature: Nature; Article Type: Biology letter
DOI: 10.1038/nature13991

Fig. 3

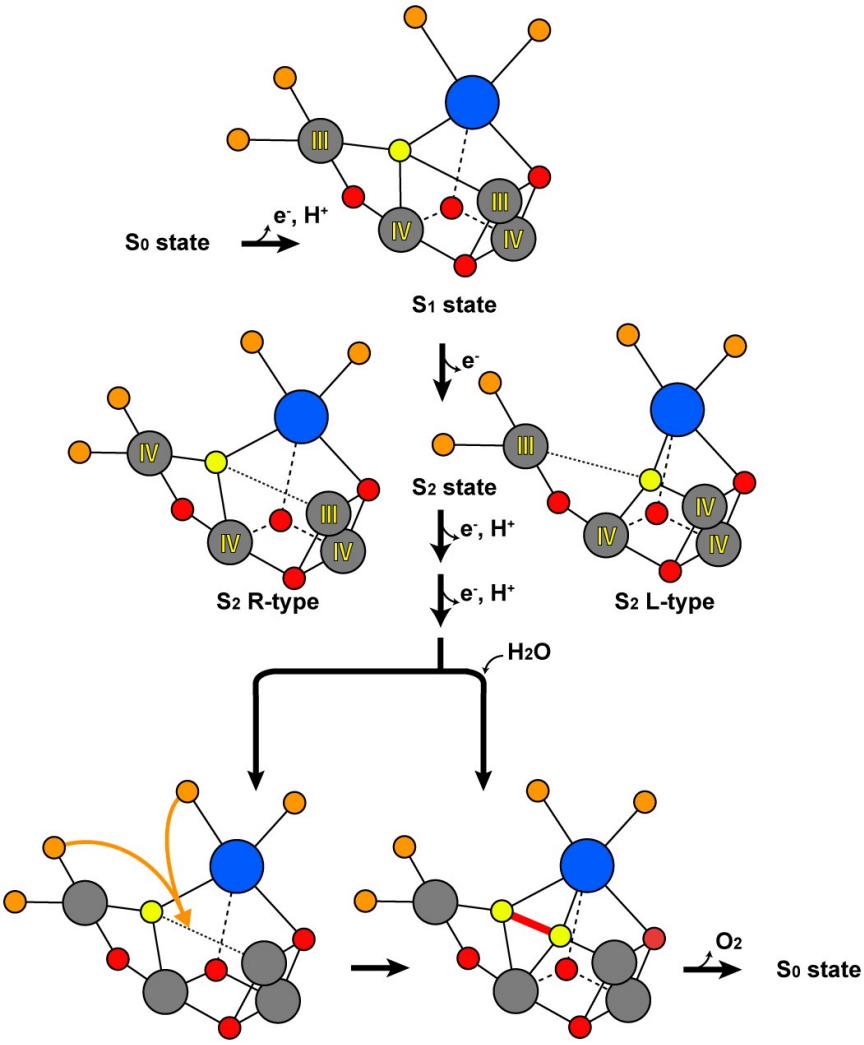

ONLINE METHODS

Pulse parameters of SACLA

The pulse parameters of SACLA were as follows: pulse duration, 10 fs or shorter; pulse flux, 2.6×10^{10} photons; photon energy, 10.0 keV; beam size, 4.0 (H) × 2.5 (V) μm^2 (FWHM) at a position 20 mm downstream from the focal position of the X-ray beam; pulse frequency, 30 Hz.

Preparation of crystals of *T. vulcanus* PSII in the S_1 state

Highly active dimeric PSII core complexes were purified from the thermophilic cyanobacterium *T. vulcanus* and crystallized as described previously[1,31]. The crystals appeared in a few days and reached their maximum size of 1.2 × 0.5 × 0.2 mm within one week. The crystals were stored at 12 °C in the crystallization buffer[1] to which, glycerol, PEG 1,450 and PEG 5,000 MME were added gradually with an increment of 1% for each of the reagents every 30 min. When the cryoprotectant reagents reached the final concentrations of 25% glycerol, 10% PEG 1,450 and 10% PEG 5,000 MME, the crystals were quickly frozen in a nitrogen stream at 100 K. Purification, crystallization and freezing of the crystals were performed in the dark or under dim green light. Therefore, the crystals were fixed into the dark-stable S_1 state.

Evaluation of radiation damage propagation induced by XFEL pulse irradiation

Before image data collection, the distance that radiation damage induced by each XFEL pulse may propagate was evaluated by following the protocol developed by our group using PSII crystals[25]. In brief, a point on a large PSII crystal was exposed to an XFEL pulse with full intensity, followed by irradiation by weak XFEL pulses with an intensity attenuated by two orders of magnitude applied to various points separated by 1 μm to 50 μm with a step of 1 μm in both vertical and horizontal directions from the originally irradiated point. The numbers of diffraction spots of each still image obtained with the weak XFEL pulses were counted at various distances from the originally irradiated point, and the radiation damage was defined to occur when the number of diffraction spots was lower than that expected from a crystal without

prior exposure to the full intensity XFEL pulse. The distance of propagation of radiation damage determined in this way for PSII crystals was very similar to those determined for other protein crystals such as lysozyme and C*c*O, which is around 10 μm[25]. No perceptible radiation damage was detected beyond 11 μm from the irradiation point with a full intensity XFEL pulse. Thus we estimated that as long as each irradiation point was spatially separated by 15 μm, they would not affected by other XFEL pulses and the diffraction images would be essentially identical to the ones from intact PSII crystals. In order to ensure a complete avoidance of radiation damage from adjacent XFEL pulses, we adopted a distance of 50 μm (an additional 35 μm 'safety margin' was used) between each irradiation point to collect consecutive still images from the large PSII crystals.

Diffraction experiments

All images were collected at beamline 3 of SACLA. The very strong X-ray pulse of SACLA at its focused position produced physical damage in crystals placed at that focus; some cracked or burst, making data collection difficult. To avoid such damage, the samples were set at a position 20 mm downstream from the focal position of the X-ray beam to reduce the flux density of XFEL pulses irradiated onto the crystals. This basically eliminated physical damage, thereby enabling more efficient data collection.

Still diffraction images were recorded from the large PSII crystals sequentially. Before the irradiation by an XFEL pulse, the crystal was moved by at least 50 μm and rotated by 0.2° (Extended Data Fig. 1a, b). This stepwise rotation was aimed to record consecutive still diffraction images so that they could be processed in the same manner as the conventional oscillation diffraction method. Here, the size of the rotation step should be smaller than one-third of the crystal mosaicity to ensure the consecutiveness of the images based on the studies using crystals of lysozyme and C*c*O[25]. As the typical mosaicity of the PSII crystals was 0.60° to 0.80°[1], a 0.2° step was adequate.

Processing of the diffraction images

Some of the images recorded had significantly lower or higher intensities than typical images, probably due to fluctuations in the XFEL pulses. This situation was more severe for the first half of the images of data set 1 than for the rest of data set 1 and data set 2 because of a larger variation in the pulse intensities during collection of the first half of the images of data set 1. The intensities of the first half images of data set 1 were therefore scaled for each crystal on the basis of the I_0 values from an X-ray beam monitor placed in the optics hutch. The standard deviations of the averaged pixel values in the groups derived from the same crystal decreased by 30% after the scaling process (Extended Data Fig. 6a, b). Among these images, (1) the images that showed characteristics of 'not single' or 'cracked' crystals, or (2) a block of images that had a significant discontinuity in the course of the crystal rotation that made the data processing as continuous rotational images impossible, were not processed. In these cases, we restarted the diffraction experiments with a new crystal to cover all the unique reflections in the asymmetric unit of the reciprocal space. The images selected based on these criteria were processed with the programs ipmosflm and scala in CCP4[32]. The final images used for structural refinement were selected as follows: we discarded the 'block' of processed images whose diffraction limit was lower than 2.5 Å resolution, or the ones that made the statistics worse significantly. Those images were selected one-by-one by eye. Since we collected multiple images at similar rotational angles with multiple crystals, the selection of images with resolution higher than 2.5 Å did not affect the completeness of our data as shown in Extended Data Table 1.

The total dose was calculated with the program RADOSE[33], which showed that the total dose absorbed and photon density were 1.4 MGy and 0.26×10^{10} photons per μm^2, respectively, for each irradiation point in a crystal. This total dose and photon density was approximately equal to that each point received for the data set collected previously at the SR source[1]. The conditions and statistics for diffraction experiments are provided in Extended Data Table 1,

which showed that the unit cell constants were slightly different between the XFEL and SR data. This is because, as we have shown previously[1,31], post-crystallization treatment is very important to obtain better and isomorphous diffracting PSII crystals. Our crystals are very sensitive to cryo-conditions, and the conditions (that is, the composition of the final cryo-protectant buffer) we used in this work were slightly different from those used in the previous work. We used 25% glycerol, 10% PEG 1,450 and 10% PEG 5,000 MME for the final cryo-protectant solution, whereas 25% glycerol and 20% PEG 3000 were used in the previous cases for the SR data collection. This may be the reason for the unit cell change between the XFEL and SR data.

The *R*-factor between data set 1 and data set 2 is 0.177. This is larger than the *R*-factors among sub-data sets obtained from the same data sets, which is typically less than 0.05 based on our studies at synchrotron sources. This is largely due to an insufficient isomorphism among the crystals grown from different batches of samples between data sets 1 and 2, although we cultured, purified and crystallized the sample using the same protocols.

Structural determination

The initial phase information up to 3.0 Å resolution was obtained by the molecular replacement method with the Phaser program in CCP4[32] using the 1.9 Å resolution structure (PDB ID 3ARC) as a search model, in which all of the cofactors including OEC, amino acid residues coordinating OEC and water molecules were omitted. The phases obtained were then extended and improved using the program DM in CCP4[32]. Because the XFEL structure and the SR structure were essentially equivalent at 3.0 Å resolution, the phases obtained after density modification should not be biased by the SR structure. The model was built manually using COOT[34] in the resulting electron density map ($F_o \times \exp(i\alpha_{DM})$). The structural refinement was carried out with Phenix[35]. OEC was not included in the structural model until the final stage of the structural refinement which is described in the next section.

Refinement of the OEC structure

The positions of four manganese atoms, one calcium atom and ligand residues were clearly visible in the $2mF_o - DF_c$ map before placement of any of these atoms (Fig. 2a), whereas the positions of the five oxo-oxygen atoms were clearly identified in the $mF_o - DF_c$ map after placement of the manganese and calcium atoms as shown in Fig. 2a. When we started to build the OEC model, we placed the Mn_4CaO_5 cluster manually, and performed the structural refinement with strict restraints for bond distances (Mn–O and Ca–O) that were taken exactly from the SR structure (PDB ID 3ARC). This refinement resulted in a shortening of all Mn–Mn distances compared to the SR structure, and some of the positions of the refined oxo-oxygen atoms using 'the strict SR structure restraints' for Mn–O and Ca–O distances did not agree well with the positions identified from the $mF_o - DF_c$ map calculated before placing any oxo-oxygen atoms. Moreover, the refinement with 'the strict SR structure restraints' for Mn–Mn distances but loose restraints for Mn–O and Ca–O led to a significant increase in the residual density in the $mF_o - DF_c$ map. Therefore, although the overall shape was very similar, the OEC in the XFEL structure was apparently different from that in the SR structure in terms of the positions of the individual atoms. Therefore, the refinements were accomplished with rounds of geometry optimizations in which the optimal geometry for the Mn_4CaO_5 cluster was determined from the previous refined structure under loose constraints for bond distances of Mn–O and Ca–O. Then the restrained refinement was performed successively using the modified 'new' library for the bond distances. This geometry optimization procedure was repeated several times until no further changes in the bond distances were observed, and the correctness of the structural refinements was confirmed by checking the decrease in the residual density of the $mF_o - DF_c$ maps. In the final refined structure obtained, all of the oxo-oxygen atoms existed in the central position of the density in the $mF_o - DF_c$ map calculated before placing them, and the residual electron density in the $mF_o - DF_c$ map was minimized. The average and standard deviation of the distances Mn–Mn, Mn–Ca, Mn–O and Mn–ligand were calculated from four independent

PSII monomers (two dimers in each data set) and are listed in Extended Data Table 3, which shows that they had very small deviations, therefore enabling comparisons of the inter-atomic distances between the XFEL and SR structures.

31. Shen, J. R. & Kamiya, N. Crystallization and the crystal properties of the oxygen-evolving photosystem II from *Synechococcus vulcanus*. *Biochemistry* **39,** 14739–14744 (2000).

32. Collaborative Computational Project, Number 4. The CCP4 suite: programs for protein crystallography. *Acta Crystallogr. D* **50,** 760–763 (1994).

33. Murray, J., Garman, E. & Ravelli, R. X-ray absorption by macromolecular crystals: the effect of wavelength and crystal composition on absorbed dose. *J. Appl. Crystallogr.* **37,** 513–522 (2004).

34. Emsley, P. & Cowtan, K. Coot: model-building tools for molecular graphics. *Acta Crystallogr. D* **60,** 2126–2132 (2004).

35. Adams, P. D. *et al.* PHENIX: a comprehensive Python-based system for macromolecular structure solution. *Acta Crystallogr. D* **66,** 213–221 (2010).

Extended Data Figure 1 | Diffraction experiment using the XFEL beam at SACLA. a, Schematic drawing of the diffraction experiment. Still diffraction images were recorded from different points on large PSII crystals. The crystals were rotated by 0.2° between each image over a range of 180°. Adjacent irradiation points were separated by 50 μm in the horizontal direction for any rotational angle. Translation in the vertical direction was varied depending on the rotational angle, so that the irradiation points were also separated by 50 μm in the vertical direction. **b**, A picture of the PSII crystal in a cryo-loop after the XFEL diffraction experiment. Note that the path where the XFEL beam passed through became hollowed out, and resulted in footprints of the irradiation points, which were well separated.

Extended Figure 2 | A diffraction image from a PSII crystal obtained with the XFEL beam. A typical diffraction image is shown; the boxed area at the right is shown enlarged in the inset, where diffraction spots at the maximum resolution are visible.

Extended Data Figure 3 | Anomalous signals of the metal ions obtained with the XFEL beam. Shown are anomalous difference Fourier maps contoured at 5σ distributions. **a**, Manganese atoms of the OEC. **b**, The non-haem iron in the acceptor side between Q_A and Q_B.

Extended Data Figure 4 | Coordination environment of Mn1D, Mn2C, Mn3B and Mn4A. The ligand environment of **a**, Mn1D, **b**, Mn2C, **c**, Mn3B and **d**, Mn4A are drawn in stereo view. The ligand bonds involving O5 coordination are slightly longer than the others in both Mn1D and Mn4A. Note that Mn1D is in a pseudo-five-coordinated, trigonal bipyramidal geometry with additional weak interaction to O5. Colour code: grey, manganese; green, carbon; blue, nitrogen; red, oxo-oxygen; yellow, O5; orange, water.

Extended Data Figure 5 | Jahn-Teller axes on Mn1D and Mn4A. The ligand environment of Mn1D and Mn4A are drawn in a stereo view. Based on the longer ligand bonds involving the O5 coordination as shown in Extended Data Fig. 4a, d, two possible Jahn–Teller axes were assigned which are approximately parallel. Colour codes are the same as those in Extended Data Fig. 4.

Light blue lines indicate two Jahn–Teller axes found in the OEC in the S_1 state. **a**, View direction almost orthogonally oriented relative to the two Jahn–Teller axes. **b**, View direction rotated by 90° from **a**.

Extended Data Figure 6 | Scaling of the raw images. Standard deviations of the average pixel values calculated in the group belonging to the same crystal before and after scaling are plotted. *X* and *Y* axes indicate standard deviations obtained before and after scaling, respectively. Red line in the plot represents the relationship $Y = X$. **a**, Plot of the images collected during the first half of the beam time (including the first half of the images for data set 1). **b**, Plot of the images collected during the last half of the beam time (including the rest of the images for data set 1 and all of the images for data set 2).

Extended Data Table 1 | Data collection and refinement statistics with the XFEL beam (data set 1 and data set 2) in comparison with the SR data

*Values in parentheses indicate those for the highest resolution shells.

†R_{sym} was calculated with scala in CCP4[32] for data set 1 and data set 2, R_{mrg} was calculated with scalepack in HKL2000 for the SR data[1].

$$‡R_{pim} = \sum_{hkl}\left[1/(N-1)\right]^{1/2}\sum_i\left|I_i(hkl)-I(hkl)\right| \Big/ \sum_{hkl}\sum_i I_i(hkl)$$

§CC1/2 is the correlation coefficient between two random half data sets.

[Π]Calculated with MolProbility.

Extended Data Table 2 | *B*-factor values of the individual atoms in the OEC of the XFEL structures

The individual absolute *B*-factor values of Mn, Ca and O atoms in the Mn_4CaO_5 cluster of both A and B monomers in the two XFEL structures (data set 1 and data set 2) are shown, together with the average *B*-factors calculated from four PSII monomers. For comparison, the *B*-factors in the SR structure are also shown.

Extended Data Table 3 | Mn–Mn, Mn–Ca, Mn–O, Mn–water, Ca–O, Ca–water, O5–water and ligand distances of the OEC in each PSII monomer of the two XFEL structures.

A and B represent distances in two monomers of two independent dimer structures (data set 1 and data set 2) obtained by XFEL crystallography, and the average distances and standard deviations are calculated from the four monomers. For comparison, the average distances from the SR structure are also shown.

*Residue from CP43.

Extended Data Table 4 | Assignment of valences of individual manganese atoms in the OEC in the S_1 state based on average ligand distance and distribution of Jahn–Teller axes

Shown are the average distances for the pair of ligands along with the same line of axis in the six-coordination geometry, together with their deviations from the average distance. The valence of each Mn atom was assigned based on the average ligand distance and the existence of the possible Jahn–Teller axis.

*Plausible Jahn-Teller axis

†Possible Jahn–Teller axis

‡Residue from CP43.

Publisher: NPG; Journal: Nature: Nature; Article Type: Biology letter
DOI: 10.1038/nature13991

Extended Data Figure 1

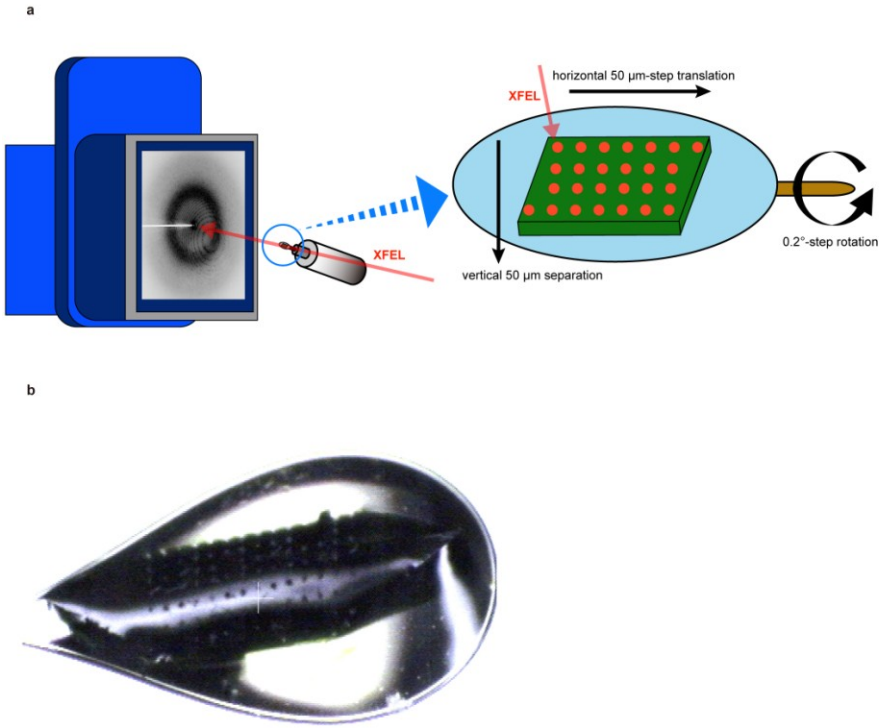

Publisher: NPG; Journal: Nature: Nature; Article Type: Biology letter
DOI: 10.1038/nature13991

Extended Data Figure 2

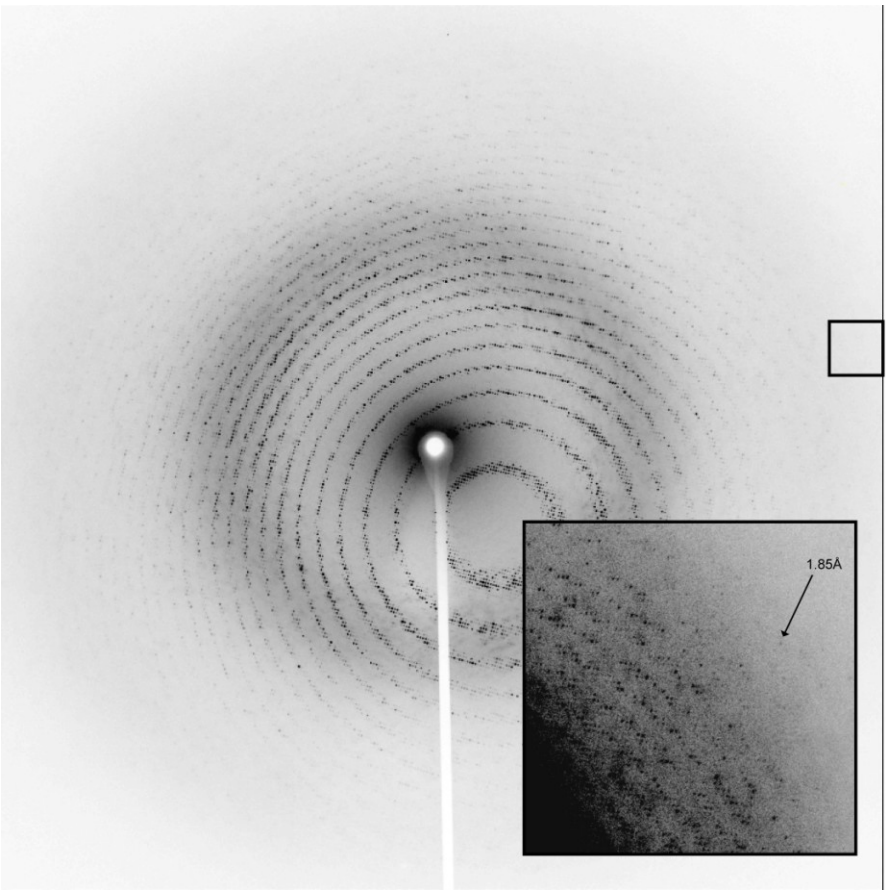

Publisher: NPG; Journal: Nature: Nature; Article Type: Biology letter
DOI: 10.1038/nature13991

Extended Data Figure 3

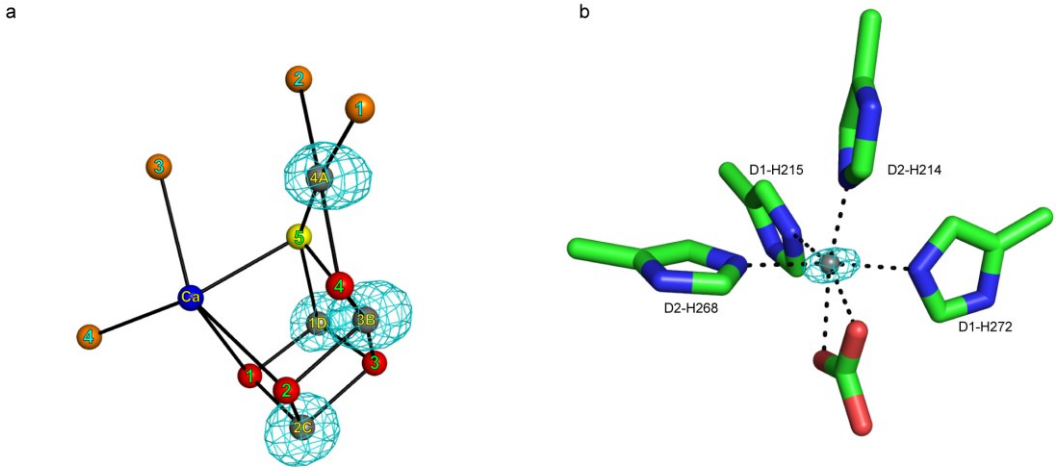

Publisher: NPG; Journal: Nature: Nature; Article Type: Biology letter
DOI: 10.1038/nature13991

Extended Data Figure 4

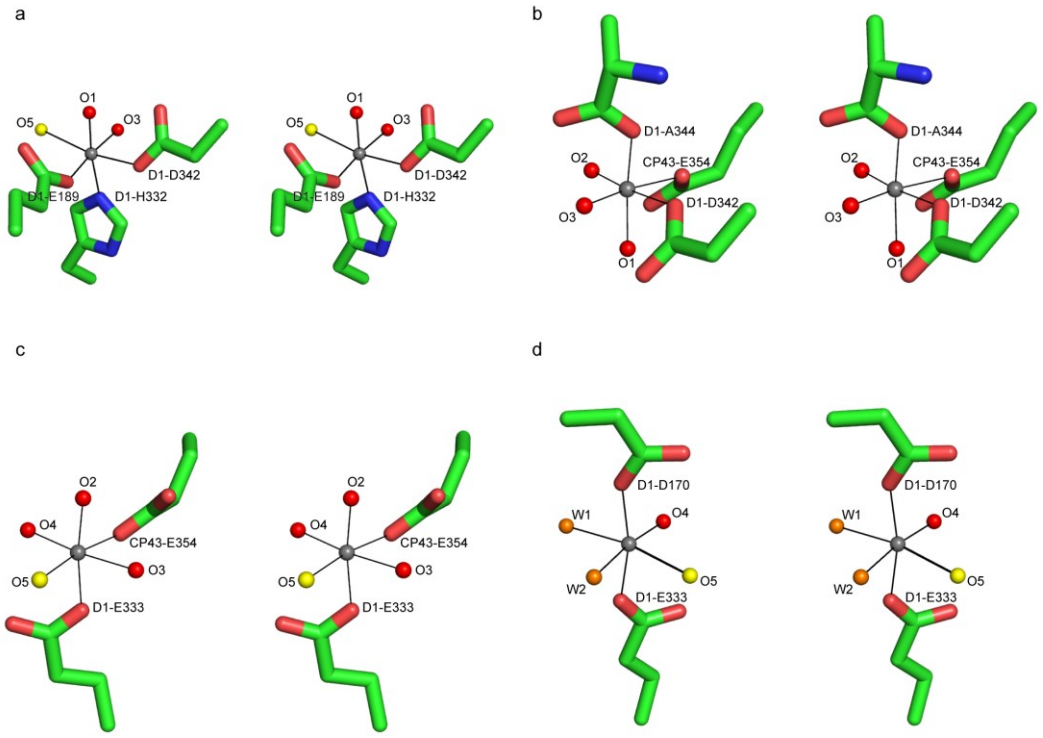

Publisher: NPG; Journal: Nature: Nature; Article Type: Biology letter
DOI: 10.1038/nature13991

Extended Data Figure 5

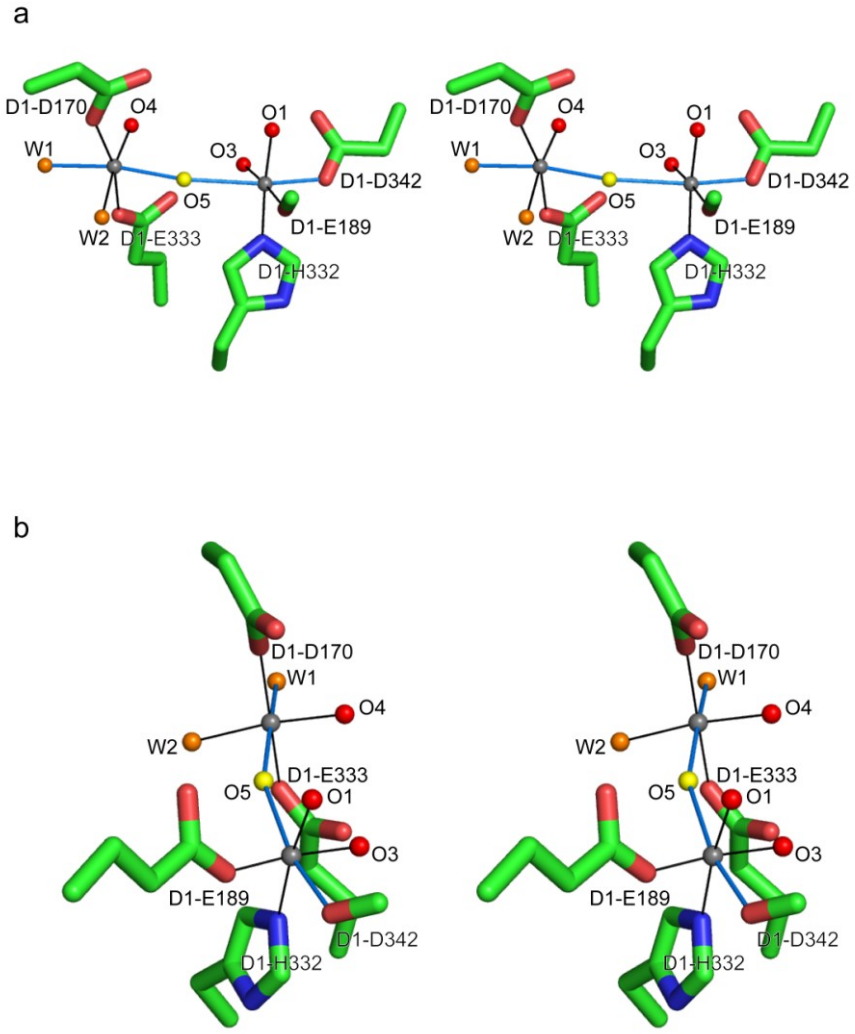

Publisher: NPG; Journal: Nature: Nature; Article Type: Biology letter
DOI: 10.1038/nature13991

Extended Data Figure 6

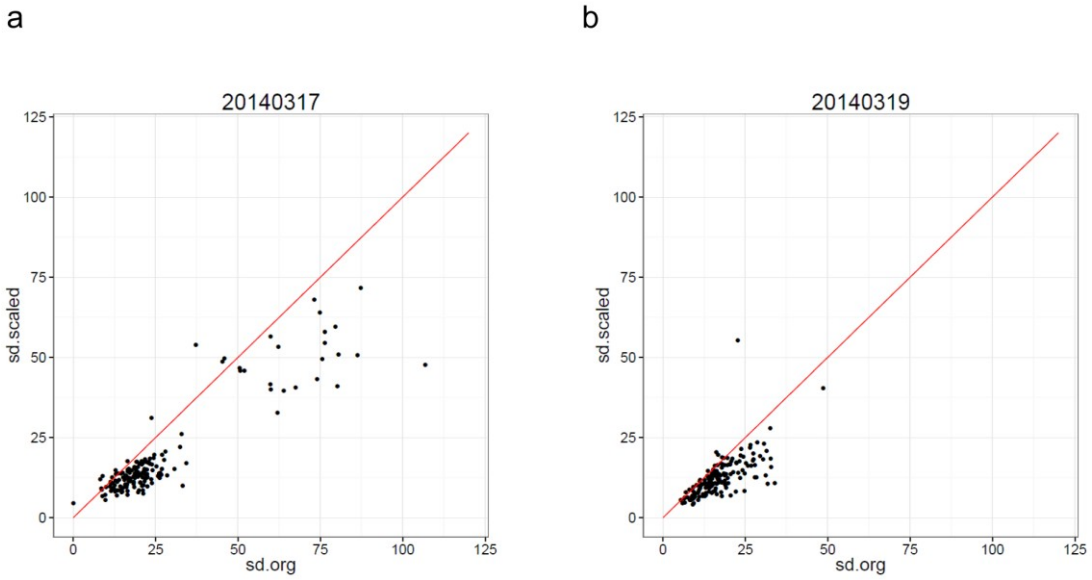

Extended Data Table 1 | Data collection and refinement statistics with the XFEL beam (dataset-1 and dataset-2) in comparison with the SR data.

	XFEL (dataset-1)	XFEL (dataset-2)	SR
Experimental conditions			
Wavelength / Å	1.24357	1.24357	0.90000
Osillation width / deg.	0	0	0.2
Step width / deg.	0.2	0.2	
Total dose / Gy	1.4E+06	1.4E+06	7.4E+05
Photon density per μm^2	2.6E+09	2.6E+09	2.8E+09
No. of screened crystals	254	82	1
No. of total collected images	5,592	2,058	900
No. of processed images	1,643	1,167	900
No. of images used for refinement	658	680	900
Data collection statistics			
Space group	$P2_12_12_1$	$P2_12_12_1$	$P2_12_12_1$
Unit cell / Å	a=123.8, b=230.0, c=288.3	a=123.8, b=230.0, c=288.5	a=122.2, b=228.5, c=286.4
Resolution / Å	62.7 - 1.95 (2.06 - 1.95)*	62.3 - 1.95 (2.06 - 1.95)*	50 - 1.90 (1.97 - 1.90)*
No. of reflections	585,462 (83,527)*	586,125 (82,791)*	622,012
Completeness / %	98.7 (97.0)*	98.4 (95.9)*	99.6 (99.7)*
Redundancy	4.9 (4.6)*	5.1 (4.7)*	7.4 (6.7)*
R_{sym} / R_{mrg}†	0.330 (1.184)*	0.294 (1.579)*	0.060 (0.773)*
R_{pim}‡	0.172 (0.634)*	0.192 (1.070)*	
CC1/2§	0.919 (0.166)*	0.929 (0.362)*	
I/σ (I)	3.5 (0.9)*	3.1 (0.6)*	21.6 (2.6)*
Refinement statistics			
R factor	0.198	0.188	0.174
R free	0.238	0.225	0.201
Average B (overall) / $Å^2$	34.3	35.9	35.2
Average B (OEC) / $Å^2$	22.2	25.0	25.6
RMSD bond length / Å	0.009	0.009	0.010
RMSD bond angle / deg.	1.44	1.44	3.05
Ramachandran plot‖			
Favored / %	97.7	97.9	98.4
Allowed / %	2.1	2.0	1.5
Outliers / %	0.2	0.1	0.1

*Values in parenthesis indicate those for the highest resolution shells.

†R_{sym} was calculated with scala for dataset 1 and dataset 2, R_{mrg} was calculated with scalepack for the SR data.

‡$R_{pim} = \sum_{hkl}[1/(N-1)]^{1/2}\sum_i|I_i(hkl) - \langle I(hkl)\rangle| / \sum_{hkl}\sum_i I_i(hkl)$

§CC1/2 is the correlation coefficient between two random half data sets.

‖Calculated with MolProbility.

Extended Data Table 2 | B-factor values of the individual atoms in OEC of the XFEL structures. The individual absolute B-factor values of Mn, Ca and O atoms in the Mn_4CaO_5-cluster of both A and B monomers in the two XFEL structures (dataset-1 and dataset-2) are shown, and the average B-factors were calculated from four PSII monomers. For comparison, the B-factors in the SR structure were also shown.

	Dataset-1		Dataset-2		XFEL		SR		
	A	B	A	B	Average	std	A	B	Average
Mn1D	20.2	24.7	21.4	27.4	**23.4**	**3.3**	22.6	26.0	**24.3**
Mn2C	22.1	22.9	23.2	25.3	**23.4**	**1.4**	22.9	26.7	**24.8**
Mn3B	19.6	21.5	22.1	25.0	**22.0**	**2.2**	23.5	25.5	**24.5**
Mn4A	21.5	22.8	24.2	25.2	**23.4**	**1.6**	26.3	28.7	**27.5**
Ca	28.3	34.0	32.5	37.4	**33.0**	**3.8**	24.6	27.5	**26.0**
O1	21.0	20.3	28.1	24.0	**23.3**	**3.6**	22.5	25.1	**23.8**
O2	24.2	19.6	23.6	22.9	**22.6**	**2.1**	25.2	27.3	**26.3**
O3	24.6	24.0	21.0	35.8	**26.3**	**6.5**	23.3	27.1	**25.2**
O4	20.0	18.9	23.8	20.3	**20.7**	**2.1**	26.6	27.7	**27.2**
O5	15.1	18.8	16.7	20.2	**17.7**	**2.3**	24.1	28.1	**26.1**
overall (OEC)	21.6	22.7	23.7	26.4	**23.6**	**2.0**	24.2	27.0	**25.6**

Publisher: NPG; Journal: Nature: Nature; Article Type: Biology letter
DOI: 10.1038/nature13991

Extended Data Table 3 | Mn-Mn, Mn-Ca, Mn-O, Mn-water, Ca-O, Ca-water, O5-water and ligand distances of OEC in each PSII monomers of the two XFEL structures. A and B represent distances in two monomers of two independent dimer structures (dataset-1 and dataset-2) obtained by the XFEL crystallography, and the average distances and standard deviations are calculated from the four monomers. For comparison, the average distances from the SR structure are also shown.

	Dataset-1		Dataset-2		XFEL		SR
	A	B	A	B	Average	std	Average
Mn1D-Mn2C	2.67	2.51	2.74	2.68	**2.65**	**0.10**	2.8
Mn1D-Mn3B	3.24	3.18	3.27	3.10	**3.20**	**0.08**	3.3
Mn1D-Mn4A	4.95	4.97	4.97	4.89	**4.95**	**0.04**	5.0
Mn2C-Mn3B	2.70	2.67	2.73	2.71	**2.70**	**0.03**	2.9
Mn2C-Mn4A	5.17	5.18	5.21	5.27	**5.21**	**0.04**	5.4
Mn3B-Mn4A	2.86	2.83	2.88	2.91	**2.87**	**0.03**	3.0
Mn1D-Ca	3.51	3.45	3.49	3.43	**3.47**	**0.04**	3.5
Mn2C-Ca	3.35	3.29	3.33	3.32	**3.32**	**0.03**	3.4
Mn3B-Ca	3.47	3.39	3.41	3.33	**3.40**	**0.06**	3.4
Mn4A-Ca	3.76	3.86	3.71	3.76	**3.77**	**0.06**	3.8
Mn1D-O1	1.85	1.80	1.81	1.73	**1.80**	**0.05**	1.9
Mn1D-O3	1.94	1.93	1.80	1.80	**1.87**	**0.08**	1.8
Mn1D-O5	2.70	2.72	2.70	2.69	**2.70**	**0.01**	2.6
Mn2C-O1	1.83	1.72	1.88	1.83	**1.82**	**0.07**	2.1
Mn2C-O2	1.90	1.74	1.83	1.83	**1.83**	**0.07**	2.1
Mn2C-O3	1.95	2.06	2.01	2.07	**2.02**	**0.06**	2.1
Mn3B-O2	1.78	1.81	2.00	2.00	**1.90**	**0.12**	1.9
Mn3B-O3	2.08	1.99	2.14	2.02	**2.06**	**0.07**	2.1
Mn3B-O4	1.91	1.92	1.89	1.88	**1.90**	**0.02**	2.1
Mn3B-O5	2.17	2.01	2.32	2.30	**2.20**	**0.14**	2.4
Mn4A-O4	1.94	2.04	2.05	2.03	**2.02**	**0.05**	2.1
Mn4A-O5	2.32	2.30	2.38	2.33	**2.33**	**0.03**	2.5
Mn4A-W1	2.34	2.15	2.26	2.24	**2.25**	**0.08**	2.2
Mn4A-W2	2.15	1.97	2.14	2.14	**2.10**	**0.09**	2.2
Ca-O1	2.57	2.61	2.64	2.61	**2.61**	**0.03**	2.4
Ca-O2	2.67	2.58	2.73	2.69	**2.67**	**0.06**	2.5
Ca-O5	2.59	2.60	2.43	2.52	**2.54**	**0.08**	2.7
Ca-W3	2.61	2.60	2.59	2.59	**2.60**	**0.01**	2.4
Ca-W4	2.51	2.49	2.44	2.42	**2.47**	**0.04**	2.5
O5-W2	3.07	2.91	3.08	2.95	**3.00**	**0.09**	3.1
O5-W3	3.21	3.25	2.98	3.05	**3.12**	**0.13**	3.1
W2-W3	3.38	3.17	3.23	3.27	**3.26**	**0.09**	3.3
Mn1D-OE2 (Glu189)	1.78	1.76	1.81	1.81	**1.79**	**0.02**	1.9
Mn1D-NE2 (His332)	2.08	2.11	2.13	2.16	**2.12**	**0.03**	2.2
Mn1D-OD2 (Asp342)	2.16	2.19	2.26	2.25	**2.22**	**0.05**	2.3
Mn2C-OD1 (Asp342)	2.14	2.07	2.16	2.15	**2.13**	**0.04**	2.2
Mn2C-OXT (Ala344)	1.92	1.85	1.97	1.86	**1.90**	**0.06**	2.0
Mn2C-OE1 (Glu354*)	2.12	2.19	2.10	2.09	**2.13**	**0.05**	2.2
Mn3B-OE1 (Glu333)	2.03	2.08	2.04	2.08	**2.06**	**0.03**	2.1
Mn3B-OE2 (Glu354*)	2.12	2.12	2.16	2.12	**2.13**	**0.02**	2.2
Mn4A-OD2 (Asp170)	2.05	2.08	2.00	2.00	**2.03**	**0.04**	2.1
Mn4A-OE2 (Glu333)	2.07	2.10	2.06	2.10	**2.08**	**0.02**	2.2
Ca-OD1 (Asp170)	2.28	2.46	2.34	2.34	**2.36**	**0.08**	2.4
Ca-O (Ala344)	2.41	2.43	2.43	2.43	**2.43**	**0.01**	2.5

*Residue from to CP43.

Extended Data Table 4 | Assignment of the valances for the individual manganese atoms in OEC in the S_1-state based on the average ligand distances and Jahn-Teller axes distribution. The average distances for the pair of ligands along with the same axis in the six-coordination geometry, together with their deviations from the average distances were calculated. The valance of each Mn atom was assigned based on the average ligand distances and existence of the possible Jahn-Teller axis.

Axis pair of the ligands	Average distance (Å)	Deviation from the average (%)	Assigned valance
Mn1D			
O1/NE2 (His332)	1.96	-5.9	
O3/OE2 (Glu189)	1.83	-12.2	
O5/OD2* (Asp342)	2.46	18.1	
Average	**2.08**		**III**
Mn2C			
O1/OE1 (Glu354‡)	1.97	0.0	
O2/OD1 (Asp342)	1.98	0.4	
O3/OXT (Ala344)	1.96	-0.4	
Average	**1.97**		**IV**
Mn3B			
O2/OE1 (Glu333)	1.98	-3.1	
O3/O4	1.98	-3.0	
O5/OE2† (Glu354‡)	2.17	6.1	
Average	**2.04**		**IV**
Mn4A			
O4/W2	2.06	-3.6	
O5/W1†	2.29	7.3	
OD2 (Asp170)/OE2 (Glu333)	2.06	-3.6	
Average	**2.14**		**III**

*Plausible Jahn-Teller axis

†Possible Jahn-Teller axis

‡Residue from to CP43.